JCTC Journal of Chemical Theory and Computation

Article

pubs.acs.org/JCTC

A First-Principles Time-Dependent Density Functional Theory Framework for Spin and Time-Resolved Angular-Resolved Photoelectron Spectroscopy in Periodic Systems

Umberto De Giovannini,[*,†,§] Hannes Hübener,[*,†] and Angel Rubio[*,†,‡,⊥]

[†]Nano-Bio Spectroscopy Group, University of the Basque Country UPV/EHU, Avenida de Tolosa 72, 20018 San Sebastian, Spain

[‡]Max Planck Institute for the Structure and Dynamics of Matter, Luruper Chaussee 149, 22761 Hamburg, Germany

[⊥]Center for Free-Electron Laser Science and Department of Physics, University of Hamburg, Luruper Chaussee 149, 22761 Hamburg, Germany

[§]Dipartimento di Fisica e Chimica, Università degli Studi di Palermo, Via Archirafi 36, I-90123 Palermo, Italy

ABSTRACT: We present a novel theoretical approach to simulate spin, time, and angular-resolved photoelectron spectroscopy (ARPES) from first-principles that is applicable to surfaces, thin films, few layer systems, and low-dimensional nanostructures. The method is based on a general formulation in the framework of time-dependent density functional theory (TDDFT) to describe the real time-evolution of electrons escaping from a surface under the effect of any external (arbitrary) laser field. By extending the so-called t-SURFF method to periodic systems one can calculate the final photoelectron spectrum by collecting the flux of the ionization current trough an analyzing surface. The resulting approach, that we named t-SURFFP, allows us to describe a wide range of irradiation conditions without any assumption on the dynamics of the ionization process allowing for pump−probe simulations on an equal footing. To illustrate the wide scope of applicability of the method we present applications to graphene, monolayer, and bilayer WSe_2, and hexagonal BN (hBN) under different laser configurations.

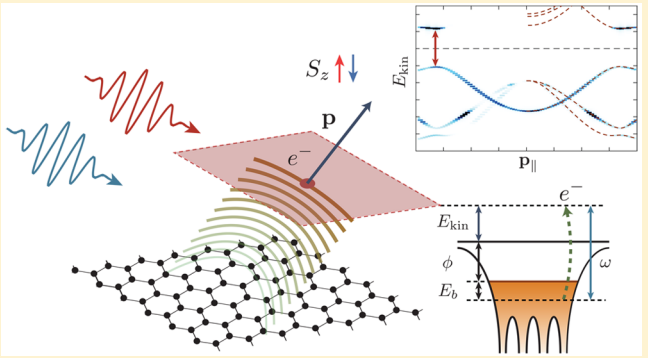

INTRODUCTION

Angular resolved photoelectron spectroscopy is one of the most prominent and mature techniques employed to probe the electronic properties of crystalline materials. In its most traditional application it allows to directly map band dispersion and Fermi surfaces of solids from the energy and momentum distribution of the escaping electrons.[1,2]

Following the advances in laser pulse generation and photoelectron detection techniques in the last years we have witnessed an increasing presence of ARPES experiments capable to resolve time and spin polarization degrees of freedom.[3,4] Time-resolved ARPES (tARPES) unlocks the time degree of freedom to study nonequilibrium dynamic of solids at the natural time scale of electronic excitations and relaxations.[5−9] Resolving the spin polarization of photoelectrons with spin ARPES (sARPES) provides additional information on the spin character of the sample.[10−13] Exploring these new dimensions offers unprecedented opportunities to test our current understanding of matter.

Currently, the most common theoretical approaches to calculate ARPES are based on the one step-model in which electron photoemission is treated as a unique coherent process that includes all the scattering events.[14] This is in contrast to the simpler three-step model in which ionization is divided into three separate processes.[15] These approaches, largely based on many-body perturbation theory formulated in terms of Green's function, proved to be successful in many relevant cases.[16−19] However, the perturbative approach underlying these methods is not suitable to describe tARPES.[20] Including the time degree of freedom needed for tARPES requires a real time approach which, in the many-body context, is provided only by Keldysh Green's function theory. Efforts in this direction are still scarce and largely reduced to applications with model-Hamiltonians,[21,22] and current attempts to formulate the problem under the one-step model are still at the formal level.[23]

In this paper we propose a completely different and computationally efficient approach based on a real-space real-time formulation of TDDFT in which we obtain the ARPES spectra by directly analyzing the photoelectron current flux through a surface using the time-dependent surface flux method (t-SURFF). The t-SURFF method is a well established technique that has been successfully employed to study ionization of atoms and small molecules under strong laser fields.[24−29] This method has only recently been exported to TDDFT by some of the authors.[30] The application of t-SURFF

Received: September 12, 2016
Published: November 30, 2016

DOI: 10.1021/acs.jctc.6b00897
J. Chem. Theory Comput. 2017, 13, 265−273

to surfaces ionization dynamics is completely new, and in this paper we present the extension of the method to semiperiodic systems. We name the extended method t-SURFFP. The resulting approach is fully ab initio and capable to describe situations with any number of laser fields without making any assumption on the ionization process and at a modest computational cost. For these reasons it is naturally suited to simulate tARPES. Furthermore, in the spirit of the one-step model, scattering and surface effects are automatically included in the formalism.

The paper is organized as follows. In section 1 we present our method in the context of TDDFT and in the more general context of ARPES. We then proceed to validate our technique in section 2 where we illustrate three representative cases: graphene, WSe_2, and hBN. Finally, in section 3 we discuss our findings and present the conclusions.

Atomic units ($\hbar = e = 1$) are used throughout the paper unless otherwise specified.

1. THEORY

1.1. General. We here below briefly introduce the key concepts and quantities commonly used in the field and that we will use thought the paper.

ARPES experiments are based on electron photoemission. When a field of appropriate energy ω irradiates a material surface a fraction of the electrons, originally bound to the crystal, is released into the vacuum as shown in Figure 1a.

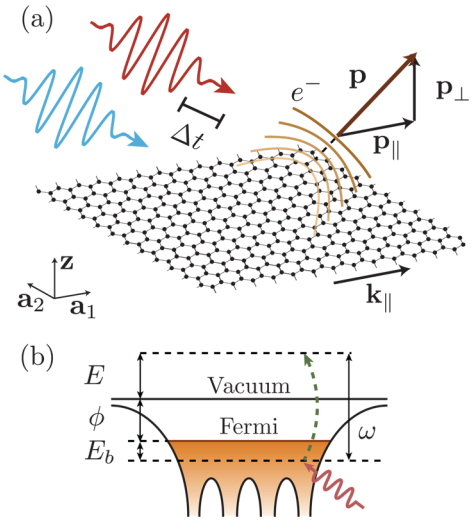

Figure 1. Schematic cartoon for the basic ingredients of tARPES. In panel a we illustrate the electron photoemission process from a surface which periodically repeats itself along the lattice vectors $\mathbf{a}_1$ and $\mathbf{a}_2$. A useful picture to guide in the interpretation of ARPES is provided by the photoelectric effect depicted in panel b.

These ionized electrons emerge with a kinetic energy distribution that depends both on the external field and the material's electronic properties. Further away, at the detector, the kinetic energy distribution is measured as a function of energy E and angle θ, to form the angular resolved photoelectron spectrum $\mathcal{P}(E, \theta)$. This spectrum can be equivalently expressed as a function of the escaping vector momentum $\mathbf{p}$, $\mathcal{P}(\mathbf{p})$. In some experiments a second stage is also capable of characterizing the spin polarization along an arbitrary axis $\mathbf{s}$ and thus of measuring $\mathcal{P}_\mathbf{s}(\mathbf{p})$. Finally, time resolution can be achieved employing two pulses delayed by a time Δt in a pump−probe setup. The time-resolved spectrum, $\mathcal{P}(\mathbf{p}, \Delta t)$, is thus obtained by composing the spectra stroboscopically measured at different delays.

Einstein's photoelectric effect[31] underlies the interpretation of the physical information contained in the photoelectron spectrum represented schematically in Figure 1b. In fact, the kinetic energy distribution of the electrons escaping the material follows the energy conservation relation $E = \omega - \phi - E_b$; where $\phi > 0$ is the work function, the minimum energy required to promote one electron into the vacuum, and $E_b > 0$ is the binding energy, the band energy of the electrons relative to the Fermi level. To extract one electron from the material requires a field with $\omega > \phi$.

From energy conservation it is thus apparent that the photoelectron spectrum contains information on the energy levels of the system. If the laser field is weak enough we can assume that the electron's momentum parallel to the surface $\mathbf{k}_\parallel$—the crystal momentum—is conserved during the ionization process. This means that at the detector $\mathbf{p}_\parallel = \mathbf{k}_\parallel$ and thus that $\mathcal{P}(\mathbf{p}_\parallel, E)$, obtained from ARPES $\mathcal{P}(\mathbf{p})$ with $E = \mathbf{p}^2/2$, directly maps to the electron dispersion in the crystal, that is, the band structure.

This is the cornerstone of ARPES, but it is important to bear in mind that it is a strong idealization, useful to interpret the data, while in the reality of the experiment the picture can be more complex. Several effects present in real materials may contribute to a departure from this picture. Among the most common we mention dynamical coupling to bosonic excitations such as phonons or plasmons[32−34] and surface effects.[16,35]

In this paper we take an atomistic approach to simulate the photoemission process and include in the calculation the portion of space centered around the surface, both extending in the material and in the vacuum, that is needed to describe the process. In the next section we describe the formalism, in the framework of TDDFT, to perform such a simulation and later discuss how ARPES can be obtained from the time-dependent density.

1.2. Time-Dependent Spin-Density Functional Theory for Semiperiodic Systems. In this work we describe systems with nontrivial spin configurations derived from the presence of spin−orbit coupling, (SOC) and therefore we use spin-density functional theory (SDFT).[36]

In SDFT the fundamental variable is the 2× 2 spin-density matrix $\boldsymbol{\rho}(\mathbf{r}) = \rho_{\alpha\beta}(\mathbf{r})$ where the greek indices span the spin space $\alpha = +, -$. This matrix is defined in terms of the spinless density, or charge density, $n(\mathbf{r})$ and the magnetization vector $\mathbf{m}(\mathbf{r})$ as follows

$$\boldsymbol{\rho}(\mathbf{r}) = \frac{1}{2} n(\mathbf{r})\sigma_0 + \frac{1}{2}\mathbf{m}(\mathbf{r})\cdot\boldsymbol{\sigma} \tag{1}$$

where $\boldsymbol{\sigma} = (\sigma_x, \sigma_y, \sigma_z)$ is the 2 × 2 Pauli matrices and σ_0 is the identity matrix. From the definition it directly follows that the spinless density $n(\mathbf{r})$ can be obtained by tracing the spin-density matrix over the spin dimension $n(\mathbf{r}) = \mathrm{Tr}(\boldsymbol{\rho}(\mathbf{r}))$.

In this work we address the modeling on electrically driven systems for which the use of TDDFT is justified. For the case of time-dependent magnetic fields one should in principle use time-dependent current-DFT.[37] The central principle of TDDFT is that all observables of a time-dependent many-body system can be obtained from the knowledge of its time-dependent density alone.[38−40] Likewise in static DFT the

DOI: 10.1021/acs.jctc.6b00897
J. Chem. Theory Comput. 2017, 13, 265−273

system of interacting particles is mapped into an auxiliary noninteracting system having the same time-dependent density, the Khon–Sham (KS) system.[41] The KS system is represented by a Slater determinant composed of two-component spinors

$$\overline{\varphi}_j(\mathbf{r}) = \begin{bmatrix} \varphi_{j+}(\mathbf{r}) \\ \varphi_{j-}(\mathbf{r}) \end{bmatrix} \tag{2}$$

whose time evolution is governed by the following time-dependent KS equations (TDKS)

$$\begin{cases} i\dfrac{\partial}{\partial t}\overline{\varphi}_j(\mathbf{r}, t) = \hat{H}_{\mathrm{KS}}[\boldsymbol{\rho}](\mathbf{r})\overline{\varphi}_j(\mathbf{r}, t) \\ \hat{H}_{\mathrm{KS}}[\boldsymbol{\rho}](\mathbf{r}) = -\dfrac{1}{2}\left(\nabla - \dfrac{\mathbf{A}(t)}{c}\right)^2 \sigma_0 + V_{\mathrm{ion}}(\mathbf{r}) \\ \qquad\qquad + V_{\mathrm{KS}}[\boldsymbol{\rho}](\mathbf{r}) \end{cases} \tag{3}$$

where $\hat{H}_{\mathrm{KS}}[\boldsymbol{\rho}](\mathbf{r})$ is the KS Hamiltonian composed of the external laser field expressed as a time-dependent vector potential in the velocity gauge $\mathbf{A}(t)$ (with the electric field being $\mathbf{E}(t) = \partial\,\mathbf{A}/\partial t$), the external potential generated by the ions in the lattice $V_{\mathrm{ion}}(\mathbf{r})$, and the KS potential $V_{\mathrm{KS}}[\boldsymbol{\rho}](\mathbf{r})$. The KS potential is the sum of the classical electrostatic potential $V_{\mathrm{H}}[n](\mathbf{r})$ that only depends on the spinless density and the exchange and correlation potential $V_{\mathrm{xc}}[\boldsymbol{\rho}](\mathbf{r})$ responsible for the many-body interaction

$$V_{\mathrm{KS}}[\boldsymbol{\rho}](\mathbf{r}) = V_{\mathrm{H}}[n](\mathbf{r}) + V_{\mathrm{xc}}[\boldsymbol{\rho}](\mathbf{r}) \tag{4}$$

Nontrivial spin configurations are induced by spin–orbit coupling (SOC) whenever heavy ions are present in the crystal. In practice this introduces a term proportional to $\mathbf{L}\cdot\mathbf{S}$ in the ions' potential $V_{\mathrm{ion}}(\mathbf{r})$ that breaks spin rotational symmetry and allows for noncollinear spin configurations.

The KS Hamiltonian in eq 3 has a functional dependence on the spin-density matrix $\boldsymbol{\rho}$ which can be reconstructed from the spinors using (1) and the charge density and magnetization vector defined by

$$n(\mathbf{r}) = \sum_{j=1} \theta(\mu - \epsilon_j)\overline{\varphi}_j(\mathbf{r})^\dagger \overline{\varphi}_j(\mathbf{r}) \tag{5}$$

$$\mathbf{m}(\mathbf{r}) = \sum_{j=1} \theta(\mu - \epsilon_j)\overline{\varphi}_j(\mathbf{r})^\dagger \boldsymbol{\sigma} \overline{\varphi}_j(\mathbf{r}) \tag{6}$$

where ϵ_j is the jth eigenvalue of $\hat{H}_{\mathrm{KS}}[\boldsymbol{\rho}](\mathbf{r})$ and μ is the Fermi level obtained with the constraint that the charge density integrates to the total number of electrons: $N = \int \mathrm{d}\mathbf{r}\, n(\mathbf{r})$.

In general $\hat{H}_{\mathrm{KS}}[\boldsymbol{\rho}](\mathbf{r})$ is not diagonal in spin. The only diagonal term is the gauge-invariant kinetic operator—the first term of KS Hamiltonian in eq 3. However, in crystals composed of light atoms, for which SOC is negligible, and in the absence of a magnetic field the spin-density is collinear. This means that $\mathbf{m}(\mathbf{r})$ is constant in space and that it is possible to choose a reference frame where $\hat{H}_{\mathrm{KS}}[\boldsymbol{\rho}](\mathbf{r})$ is always diagonal. In this case we can simplify the formalism decoupling spin up and spin down to obtain two separate set of equations—the spin-polarized TDKS equations.

To describe photoemission processes from first-principles we have to describe the interface between the material and the vacuum. To this end we model a surface as a semiperiodic structure repeating itself along two directions identified by the lattice vectors $\mathbf{a}_1$ and $\mathbf{a}_2$ as in Figure 2. In the figure we indicate with $\mathbf{z}$ the nonperiodic dimension.

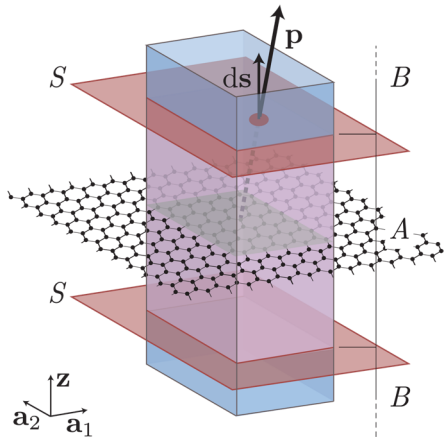

Figure 2. Scheme illustrating the geometrical model needed to simulate the ionization process in a semiperiodic system.

Owing to the periodicity of the system we can describe the infinite surface with wave functions confined to the volume $\Omega = \mathbf{a}_1 \times \mathbf{a}_2 \times \mathbb{R}$ where $\mathbf{a}_1$ and $\mathbf{a}_2$ span the planar primitive cell. On the surface, we express the wave functions as Bloch spinors $\overline{\varphi}_{j\mathbf{k}}(\mathbf{r}) = \mathrm{e}^{i\,\mathbf{k}\cdot\mathbf{r}}\,\overline{u}_{j\mathbf{k}}(\mathbf{r})$ where $\overline{u}_{j\mathbf{k}}(\mathbf{r})$ is a spinor with the periodicity of the lattice and $\mathbf{k}$ covers the first Brillouin zone (BZ) of the reciprocal space, which is bidimensional. Using Bloch spinors corresponds to exchanging

$$\left(\nabla - \frac{\mathbf{A}(t)}{c}\right)^2 \rightarrow \left(\nabla + i\mathbf{k} - \frac{\mathbf{A}(t)}{c}\right)^2 \tag{7}$$

in the KS Hamiltonian, $\hat{H}_{\mathrm{KS}}[\boldsymbol{\rho}](\mathbf{r})$, defined in eq 3. The KS equations describing the infinite surface is then cast into a set of equations for each value of $\mathbf{k}$ coupled through $\boldsymbol{\rho}(\mathbf{r})$ which can be obtained from eq 1 integrating the Bloch spinors over the first BZ in eqs 5 and 6.

1.3. The t-SURFFP Method. To derive a suitable formalism for photoemission with TDDFT in semiperiodic systems we employ the t-SURFF method.[24,25] This method was recently extended to TDDFT in finite systems[30] and we hereby present a further extension to the semiperiodic case that we name t-SURFFP.

To this end we partition the volume Ω along the nonperiodic dimension in two regions, A and B, as illustrated in Figure 2. We assume that in region A electrons are fully interacting and described by the KS Hamiltonian $\hat{H}_{\mathrm{KS}}(t)$ while in B they are noninteracting and free. In other words we ask that the time-dependent Hamiltonian governing the evolution of the system, $\hat{H}(t)$, asymptotically reduces to an exactly solvable one, $\hat{H}_{\mathrm{V}}(t)$, for all times

$$\hat{H}(t) = \begin{cases} \hat{H}_{\mathrm{KS}}(t) & \text{for } \mathbf{r} \in A \\ \hat{H}_{\mathrm{V}}(t) & \text{for } \mathbf{r} \in B \end{cases} \tag{8}$$

In our scheme $\hat{H}_{\mathrm{V}}(t)$ is the Volkov Hamiltonian governing the dynamics of N noninteracting free electrons in Ω driven by a time-dependent external field $\mathbf{A}(t)$; in the velocity gauge this is expressed by

DOI: 10.1021/acs.jctc.6b00897
J. Chem. Theory Comput. 2017, 13, 265–273

$$\hat{H}_{\mathrm{V}}(t) = \sum_{j=1}^{N} \frac{1}{2}\left[-i\nabla_j - \frac{\mathbf{A}(t)}{c}\right]^2 \sigma_0 \tag{9}$$

and is diagonal in spin-space as indicated by the presence of σ_0. Provided the vector field $\mathbf{A}(t)$ is constant in space we can solve exactly the time dependent Scrödinger equation associated with $\hat{H}_{\mathrm{V}}(t)$. For each single electron the solution can be written in the form of a plane wave spinor with momentum $\mathbf{p}$

$$\overline{\chi}_{\mathbf{p}}(\mathbf{r}, t) = \sqrt{\frac{2\pi}{a_1 a_2}}\, e^{i\mathbf{p}\cdot\mathbf{r}} e^{-i\phi(\mathbf{p},t)} \tag{10}$$

multiplied by the exponential of a time-dependent phase factor

$$\phi(\mathbf{p}, t) = \frac{1}{2}\int_0^t d\tau \left[\mathbf{p} - \frac{\mathbf{A}(\tau)}{c}\right]^2 \tag{11}$$

Each spinor is normalized on Ω which is finite along $\mathbf{a}_1$ and $\mathbf{a}_2$ but infinite along $\mathbf{z}$, and the normalization factor precisely accounts for this geometry. Further, owing to periodic boundary conditions along $\mathbf{a}_1$ and $\mathbf{a}_2$, we can decompose $\mathbf{p}$ into a sum of a k-point $\mathbf{k}$, bound to the plane of the surface, and a general reciprocal lattice vector $\mathbf{G}$: $\mathbf{p} = \mathbf{k} + \mathbf{G}$. Because of the periodicity of the system, $\mathbf{G}_{\parallel}$ assumes discrete values while $\mathbf{G}_{\perp}$ is continuos. Since the wave functions in eq 10 are not pure Volkov waves but retain information about the periodic dimensions we denote them as Bloch−Volkov waves.

When the system ionizes we can make a further assumption on the spatial distribution of the wave function. In the long time limit, after the external field has been switched of $\mathbf{A}(t > T) = 0$, we assume that each KS spinor is factorizable into a bound and a scattering component localized in A and B, respectively,

$$\overline{\varphi}_{j\mathbf{k}}(\mathbf{r}, t) = \overline{\varphi}_{j\mathbf{k},A}(\mathbf{r}, t) + \overline{\varphi}_{j\mathbf{k},B}(\mathbf{r}, t) \tag{12}$$

Under this assumption the number of electrons escaped per unit cell from A at time T can be expressed as

$$\begin{aligned} N_{\mathrm{esc}}(T) &= \int_{\Omega} dr\, n_B(\mathbf{r}, T) \\ &= \int_{\Omega} dr \int_{BZ} d\mathbf{k} \sum_{j=1} \theta_j |\overline{\varphi}_{j\mathbf{k},B}(\mathbf{r}, T)|^2 \end{aligned} \tag{13}$$

where θ_j is a shorthand for $\theta(\mu - \epsilon_j)$ as in eq 5, and $n_B(\mathbf{r},T)$ is the charge density in B.

Since the Coulomb-Volkov waves form a complete set we can expand each KS spinor as

$$\overline{\varphi}_{j\mathbf{k},B}(\mathbf{r}, t) = \int dp\, \overline{b}_j(\mathbf{p}) \chi_{\mathbf{p}}(\mathbf{r}, t) \tag{14}$$

where we defined the coefficients

$$\overline{b}_j(\mathbf{p}) \equiv \begin{bmatrix} b_{j+1/2}(\mathbf{p}) \\ b_{j-1/2}(\mathbf{p}) \end{bmatrix} \tag{15}$$

as column vectors in spin space. Inserting eq 14 into eq 13 reults in the number of escaped electrons that can be expressed in terms of the expansion coefficients $b_{j\alpha}(\mathbf{p})$ by tracing over the spin components as follows

$$N_{\mathrm{esc}}(T) = \sum_{j=1} \theta_j \sum_{\alpha=-}^{+} \int_{BZ} d\mathbf{k} \int d\mathbf{p}\, |b_{j\alpha}(\mathbf{p})|^2 \tag{16}$$

The spinless momentum-resolved photoelectron probability $\mathcal{P}(\mathbf{p})$ is thus naturally obtained from the former expansion as the derivative with respect to $\mathbf{p}$ of $N_{\mathrm{esc}}(T)$

$$\mathcal{P}(\mathbf{p}) = \frac{\partial N_{\mathrm{esc}}(T)}{\partial \mathbf{p}} = \sum_{j=1} \theta_j \sum_{\alpha=-}^{+} \int_{BZ} d\mathbf{k} |b_{j\alpha}(\mathbf{p})|^2 \tag{17}$$

To calculate $\mathcal{P}(\mathbf{p})$ we thus need an explicit form for the expansion coefficients compatible with a TDDFT formulation. This is provided by the flux of the photoelectron current through a closed surface.

Using the continuity equation we can express the number of escaped electrons as the flux of the current density $\mathbf{J}(\mathbf{r},t)$ through a surface S enclosing the system. By choosing S as in Figure 2 parallel to the system's plane we have that

$$N_{\mathrm{esc}}(T) = -\int_0^T d\tau \oint_S d\mathbf{s}\cdot\mathbf{J}(\mathbf{r}, \tau) \tag{18}$$

We are thus left with the task of connecting $\mathbf{J}(\mathbf{r},t)$ with the KS spinors. This is achieved observing that $\mathbf{J}(\mathbf{r},t)$ can be expressed as the expectation value of the single particle current density operator

$$\hat{j}(t) = \frac{1}{2}\left[\left(-i\nabla - \frac{\mathbf{A}(t)}{c}\right) + \text{c.c.}\right]\sigma_0 \tag{19}$$

over KS orbitals as follows

$$\mathbf{J}(\mathbf{r}, t) = \sum_{j=1} \theta_j \int_{BZ} d\mathbf{k}\, \langle \overline{\varphi}_{j\mathbf{k}}(t)|\hat{j}(t)|\overline{\varphi}_{j\mathbf{k}}(t)\rangle \tag{20}$$

We can then use eq 14 to expand the bra in the former equation to obtain

$$\mathbf{J}(\mathbf{r}, t) = \sum_{j=1} \theta_j \int_{BZ} d\mathbf{k} \int d\mathbf{p}\, \overline{b}_j^*(\mathbf{p}) \langle \chi_{\mathbf{p}}(t)|\hat{j}(t)|\overline{\varphi}_{j\mathbf{k}}(t)\rangle \tag{21}$$

and the complex conjugated counterpart by expanding the ket

$$\mathbf{J}(\mathbf{r}, t) = \sum_{j=1} \theta_j \int_{BZ} d\mathbf{k} \int d\mathbf{p}\, \overline{b}_j(\mathbf{p}) \langle \overline{\varphi}_{j\mathbf{k}}(t)|\hat{j}(t)|\chi_{\mathbf{p}}(t)\rangle \tag{22}$$

Finally, by inserting eqs 21 and 22 into eq 18 and directly comparing the resulting equations with eq 16 we arrive at an explicit equation for the Bloch−Volkov expansion coefficients in the form of flux integral

$$\overline{b}_j(\mathbf{p}) = -\int_0^T d\tau \oint_S d\mathbf{s}\cdot\langle \chi_{\mathbf{p}}(\tau)|\hat{j}(\tau)|\overline{\varphi}_{j\mathbf{k}}(\tau)\rangle \tag{23}$$

Further, by exposing the k-point dependence of each Bloch−Volkov spinor, we can recast the previous equation into a form containing only the periodic component of each KS orbital as

$$\overline{b}_j(\mathbf{p}) = -\int_0^T d\tau \oint_S d\mathbf{s}\cdot\langle \mathbf{G}|\hat{j}(\tau)|\overline{u}_{j\mathbf{k}}(\tau)\rangle\, e^{i\phi(\mathbf{p},\tau)} \tag{24}$$

where $|\mathbf{G}\rangle$ are planewaves of momentum $\mathbf{G}$ normalized in Ω as in eq 10. This formulation is particularly convenient for numerical implementations since it involves only the periodic spinors $\overline{u}_{j\mathbf{k}}(\tau)$ and thus it fully exploits the Bloch factorization of the KS equations discussed in section 1.2.

Equation 24 together with eq 17 provides a straightforward way to calculate the spinless momentum-resolved photoelectron probability $\mathcal{P}(\mathbf{p})$. We recall that this result was

DOI: 10.1021/acs.jctc.6b00897
J. Chem. Theory Comput. 2017, 13, 265−273

derived under the assumption (i) that the Hamiltonian of the system can be well approximated with (8) and (ii) that scattering and bound electrons are spatially well separated at all times (12). In addition, by choosing TDDFT as a working framework, we assumed that the longitudinal part of the photoelectron current is the one that contributes the most in the photoelectron spectrum. These conditions ultimately define the range of applicability of the method. They are clearly satisfied at an infinite distance from the system and close to the detectors where electrons can be safely considered free forward-moving particles, and poor in the vicinity of the surface. Positioning the sampling surface S is the only parameter controlling the accuracy of this approximation and, in practical calculations, it has to be varied until a convergence of the spectrum is achieved.

Once the expansion coefficients are calculated we can obtain the spin-density photoelectron probability $\mathcal{P}_{\alpha\beta}(\mathbf{p}) = \mathbf{P}(\mathbf{p})$ with a procedure similar to the one employed to construct the spin-density matrix of eq 1, that is, by simply substituting the spinors in the definitions of eqs 5 and 6 with $\bar{b}_j(\mathbf{p})$ and then using eq eq 1. The spin-resolved photoelectron probability polarized along the direction $\mathbf{s}$ is obtained tracing over the spin dimension as follows

$$\mathcal{P}_{\mathbf{s}}(\mathbf{p}) = \mathrm{Tr}[\mathbf{P}(\mathbf{p})\boldsymbol{\sigma}\cdot\mathbf{s}] \tag{25}$$

The spinless photoelectron probability can also be obtained tracing out the spin degrees of freedom consistently with eq 17: $\mathcal{P}(\mathbf{p}) = \mathrm{Tr}[\mathbf{P}(\mathbf{p})]$. The photoelectron spin polarization is then defined as the ratio between spin-resolved and spinless probabilities

$$\Pi_{\mathbf{s}}(\mathbf{p}) = \frac{\mathcal{P}_{\mathbf{s}}(\mathbf{p})}{\mathcal{P}(\mathbf{p})} \tag{26}$$

From the knowledge of $\mathcal{P}(\mathbf{p})$, ARPES is directly obtained by looking at the electron photoemission probability as a function of the total kinetic energy E and the parallel component of the escaping momentum $\mathbf{p}_{\parallel}$ as discussed in section 1.1: $\mathcal{P}(\mathbf{k}_{\parallel} = \mathbf{p}_{\parallel}, E = \mathbf{p}^2/2)$.

The external field $\mathbf{A}(t)$ we used to derive the t-SURFFP eq 24 and to propagate the KS eq 3 is free to assume any arbitrary temporal shape. This means that it can describe any linear combination of laser fields. Our approach thus provides a straightforward environment to simulate tARPES where the time variable is extracted trough the variation of a time-delay, Δt, between two laser pulses in a pump−probe configuration.

2. APPLICATIONS

2.1. Computational Details. We implemented the t-SURFFP method in the Octopus code.[42−44] In Octopus the TDKS equations are solved in a real-space grid and propagated in real-time. The real-space approach offers great versatility when it comes to the description of semiperiodic systems as it naturally allows the imposition of mixed boundary conditions. The real-time propagation offers additional flexibility as it consents to describe external fields with arbitrary temporal shape. In our implementation we used the exact cutoff method described in ref 45 along the nonperiodic dimension and employed nonorthogonal grids,[46] optimized according to the lattice symmetries, on the periodic ones. Our implementation is fully parallel in grid points, k-points, bands, and spin dimension. For the largest systems presented in this paper (bilayer WSe_2), we found that the distribution over only k-points and states is enough to saturate a medium-size cluster (≈1024 cores).

In the code we use a pseudopotential formalism where only valence electrons are treated explicitly. Core electrons together with the ionic potential are replaced by an effective pseudopotential such that the ionic potential is composed of a local potential, a nonlocal one, and a SOC term

$$V_{\mathrm{ion}}(\mathbf{r}) = V_{\mathrm{local}}(\mathbf{r}) + V_{\mathrm{nlocal}}(\mathbf{r}) + V_{\mathrm{SO}}\mathbf{L}\cdot\mathbf{S} \tag{27}$$

In all the calculations we used HGH pseudopotentials[47] accounting for relativistic effects only for the compounds containing W.

Further, we used the local density approximation (LDA)[48] to the exchange and correlation functional. For noncollinear spin configurations we treat the functional at the level of local spin-density approximation (LSDA) by rotating to the local reference frame where the spin density matrix is diagonal.[49]

To prevent spurious reflection on the nonperiodic edges of the cell we employed complex absorbing-potential boundary conditions.[50] We tune the absorber parameters (width and imaginary amplitude) such that the boundary is effective in the energy window of the ejected photoelectrons.[51] Owing to the presence of absorbing boundaries the total charge in the cell is not conserved over time. To avoid artifacts from charge imbalance we chose the laser intensity such that the total charge loss is negligible. In our calculations we found that a 10^{-4}% of charge loss is sufficient to provide stable results.

In the following we present applications for three different materials having an hexagonal lattice. These are all stable layered structures that are currently in the focus of extensive research and for which a considerable amount of high quality experimental data is being produced. We stress however that the computational tool we developed is by no means restricted to hexagonal crystal lattices only.

In all the simulations we used laser pulses that are zero everywhere except for $t \in [0,T]$ with

$$\mathbf{A}(t) = \boldsymbol{\epsilon} A_0 \sin\left(\frac{\pi t}{T}\right)^2 \cos(\omega t) \tag{28}$$

here $\boldsymbol{\epsilon}$ is the polarization axis, A_0 is the peak amplitude, and ω is the carrier frequency. This choice is motivated by the resemblance to the typical experimental Gaussian shape while retaining the property of being exactly zero outside a given time window—this is important to minimize the propagation time in the simulations. All the simulations have been carried out on a box of 120 au along the nonperiodic dimension and centered around each system. Along the periodic dimension the box is taken according to the primitive cell of the system. Complex absorbing potentials of 30 au width have been placed at the opposite sides of the simulation box to prevent reflections. The t-SURFFP analyzing surface was placed at 30 au from the edges right before the onset of the absorbers. The first BZ was sampled by a 12 × 12 grid of $\mathbf{k}$-points in reciprocal space for all the systems. The spectra have been obtained propagating the TDKS equations during the onset of the pulses only with a time step of $dt = 2 \times 10^{-3}$ fs. Finally the reference band structures have been calculated from the eigenvalues of a standard self-consistent ground state DFT using the very same settings as for the ARPES simulations.

2.2. Graphene. In this section we illustrate the application of t-SURFFP to simulate ARPES from graphene. To this end we ionize the system with a 50 fs laser pulse with with ω = 95

DOI: 10.1021/acs.jctc.6b00897
J. Chem. Theory Comput. 2017, 13, 265−273

eV, $\boldsymbol{\epsilon} = \mathbf{z}$, and peak intensity $I = 10^9$ W/cm^2. In an experiment this geometry corresponds to the case where the laser is grazing with respect to the surface. In our calculations we used a grid spacing of 0.36 au and a lattice constant of $a = 4.65$ au.

The results of the simulation are illustrated in Figure 3 (a) on the Γ-K-M-Γ path in the BZ (see inset). ARPES presents

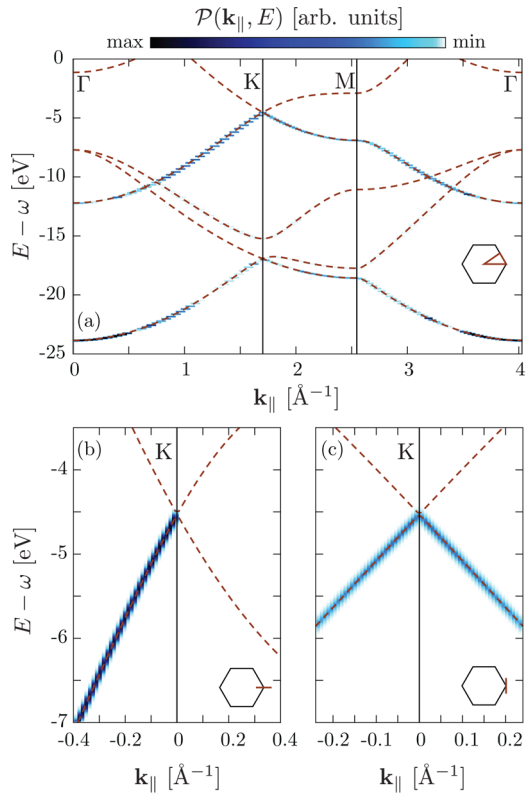

Figure 3. Graphene ARPES as obtained using a 50 fs pulse with ω = 95 eV, $\boldsymbol{\epsilon} = \mathbf{z}$, and peak intensity $I = 10^9$ W/cm^2. (a) ARPES cut along the Γ-K-M-Γ path in the BZ, (b) cut along a direction parallel to Γ-K centered in K, and (c) cut along a direction parallel to Γ−M also centered in K. In all panels the inset schematically represents the reciprocal space path on which the spectra are plotted, and the DFT band structure is overlaid in red.

intensity peaks that are positioned in excellent agreement with the DFT band structure (overlaid with red lines) and thus is in agreement with the interpretation of the ionization process in terms of the photoelectric effect.

Not all the DFT bands are visible in the spectrum. This behavior can be explained in first order time-dependent perturbation theory with Fermi's golden rule which describes the probability to excite an initial state in the material $|i\rangle$ to a final state in the continuum $|f\rangle$ in terms of the dipole matrix element $|\langle f|\hat{\mathbf{p}}\cdot\boldsymbol{\epsilon}|i\rangle|^2$. Final states that are connected with negligible matrix elements appear dark in the spectrum. The matrix element intensity effects observed in the calculation are in excellent agreement with the literature.[52]

Around the Dirac point, on the valence band close to K, graphene ARPES presents a peculiar intensity pattern. Only one branch of the Dirac cone is visible crossing K from a path along the Γ-K direction while both are visible from a direction parallel to Γ-M as shown in Figure 3b,c. This is a characteristic feature of ARPES on graphene which has been observed in many experiments[52] and that is due to the chiral character of Dirac states at the K point.[53]

In this work we do not include any dissipation channel. The finite line-width observed in ARPES is thus a direct consequence of the finite time window of the probe pulse. In principle, however, it could be possible to include dissipation, for instance, by coupling the electronics degrees of freedom with lattice vibrations using the Ehrenfest theorem.[54]

2.3. WSe_2. In this section we turn to a system with a nontrivial spin configuration and study photoemissions from the transition metal dichalcogenide WSe_2.

We probe the system with a 48 fs laser pulse polarized along $\mathbf{z}$ with carrier frequency ω = 127 eV and peak intensity $I = 10^9$ W/cm^2. We performed the simulations with a grid spacing of 0.4 au, employed a lattice constant of $a = 6.2$ au, and included semicore electrons in the pseudopotential for W. The results are presented in Figure 4 panels a and b for monolayer and bilayer, respectively.

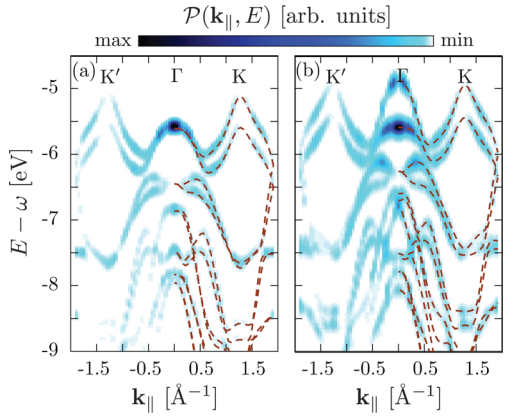

Figure 4. ARPES on WSe_2 monolayer (a) and bilayer (b). To produce the spectra we used a 48 fs laser pulse with frequency ω = 127 eV, polarization $\boldsymbol{\epsilon} = \mathbf{z}$, and peak intensity $I = 10^9$ W/cm^2. The ground state band structure is depicted in red.

As observed in the previous section the agreement between ARPES and the equilibrium band structure is excellent. In addition, the results for the bilayer in Figure 4b is in good agreement with ARPES experiments recently reported on bulk WSe_2.[55,56] The reason for such agreement is related to the surface sensibility of ARPES experiments.[9] In fact, scattering prevents photoelectrons from being ejected from the lower lying layers of the material and effectively only the topmost layers at the surface contribute to the spectrum. By comparing this spectrum to the experiments reported in refs 55 and 56, it becomes clear that the system probed by the experiment is composed of more than two layers as indicated, for instance, by the presence of an ARPES signal filling the space between the two topmost valence bands at Γ.

In monolayer WSe_2 inversion symmetry is broken. For this reason the high-symmetry points K and K′ in reciprocal space are no longer equivalent. This fact combined with a strong SOC provides a large splitting and polarization of the bands which is opposite for K and K′. Both splitting and spin polarization can be measured with sARPES as illustrated in Figure 5a. According to sARPES the topmost valence bands at K and K′ are fully spin polarized and with opposite spins. At Γ, where the bands are degenerate the spin polarization is zero. This behavior is consistent with the spin polarization of the DFT bands shown in Figure 5a where it becomes apparent that

DOI: 10.1021/acs.jctc.6b00897
J. Chem. Theory Comput. 2017, 13, 265−273

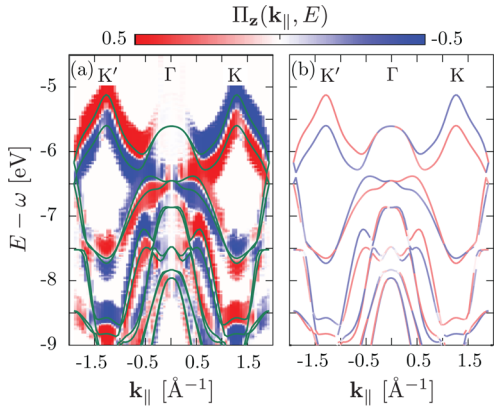

Figure 5. Spin-resolved ARPES for monolayer WSe_2: (a) $\Pi_z(\mathbf{k}_\parallel,E)$, the photoelectron spin polarization spectrum along z, overlaid with the band structure in green; (b) spin polarization of the ground state band structure. Laser parameters are the same as in Figure 4.

the zero spin-polarization at Γ emerges from degenerate bands with opposite polarizations.

2.4. Hexagonal Boron−Nitride. In this section we explore the dimension offered by tARPES and illustrate the case of monolayer hBN in a pump and probe setup.

First we probe the system in its ground state with a 24 fs UV pulse linearly polarized 45° off-plane along one of the lattice vectors $\boldsymbol{\epsilon}_\parallel = \mathbf{a}_1$ with ω = 40.8 eV, and $I = 10^{10}$ W/cm^2. The simulations have been carried out with a grid spacing 0.36 au and a lattice constant of a = 4.76 au. The resulting ARPES in Figure 6a is in good agreement with experimental data[57] and with the DFT band structure.

Next, we first pump the system with a laser pulse and probe it right after the pump is switched off. To this end we used a 20 fs in-plane pump pulse $\boldsymbol{\epsilon} = \mathbf{a}_1$ with ω = 4.46 eV, $I = 2 \times 10^{11}$ W/cm^2, and then probe with a laser delayed of Δt = 20 fs. The pump pulse is resonant with the gap at K and therefore it can excite electrons from the valence to the conduction band. This excitation is confirmed by the tARPES spectrum in Figure 6b where we observe a signal from electrons located on the conduction bands around both K and K′. This is a clear indication of a resonant population transfer from valence to conduction band and a simple demonstration of how the method presented here can be used to simulate the full dynamics of a pump−probe ARPES experiment.

3. CONCLUSIONS

In this paper we have presented the t-SURFFP method—a novel ab initio technique to simulate spin and time-resolved ARPES on semiperiodic systems based on TDDFT. This method makes no assumption on the probe pulse leaving polarization, energy, and pulse shape (envelope) free to be chosen to closely match experimental conditions. The ionization dynamics is fully simulated by time-propagation of the electronic density under the presence of the classical probe field fully accounting for electron−electron scattering, electron−ions scattering, surface image charge effects, classical screening, and other dynamical effects, thus naturally including mean free path and matrix element effects. Further the inclusion of the ionic degrees of freedoms at the level of Ehrenfest dynamics is fully compatible with the approach. Quantum mechanical exchange and correlation effects, however, are approximated within the TDDFT framework

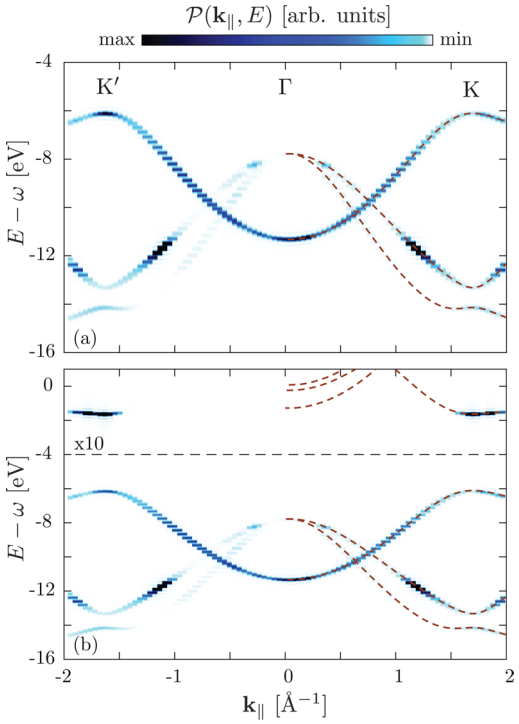

Figure 6. Pump−probe ARPES on monolayer hBN. (a) ARPES for the system in equilibrium probed by a 24 fs pulse polarized at 45° from the surface plane with $\boldsymbol{\epsilon}_\parallel = \mathbf{a}_1$, ω = 40.8 eV, and $I = 10^{10}$ W/cm^2. (b) tARPES for the system pumped with a 20 fs pulse polarized in the plane of the surface $\boldsymbol{\epsilon} = \mathbf{a}_1$ resonant with the gap at K, ω = 4.46 eV, $I = 2 \times 10^{11}$ W/cm^2, and probed by the same laser of panel a right after the pump is switched off, Δt = 20 fs. ARPES signal on the conduction band is magnified by a factor 10. The band structure is overlaid in red on both panels.

through the exchange and correlation density functional. This latter approximation imposes some limitations to systematically describe strongly correlated systems and many-body effects, but for some cases specialized functionals exists.[58−60] By accounting for the spin degree of freedom of the electrons this method also utilizes the extension of TDDFT to spin density dynamics to simulate spin-resolved ARPES measurements. The fully flexible definition of the external fields together with the first-principles propagation of the density allows the creation of complex pump−probe setups in which the electronic structure is excited separately by arbitrary pump pulses. This feature in particular allows for the first time the fully ab initio study of nonequilibrium electron dynamics under pump probe conditions via ARPES in solids with a large variety of applications.

We have thus introduced a versatile and general computational method for the ab initio study and simulation of photoemission experiments.

AUTHOR INFORMATION

Corresponding Authors

*E-mail: umberto.degiovannini@gmail.com.
*E-mail: hannes.huebener@gmail.com.
*E-mail: angel.rubio@mpsd.de.

Funding

We acknowledge financial support from the European Research Council (ERC-2015-AdG-694097), Spanish Grant (FIS2013-46159-C3-1-P), Grupos Consolidados (IT578-13), AFOSR Grant No. FA2386-15-1-0006 AOARD 144088, and European

DOI: 10.1021/acs.jctc.6b00897
J. Chem. Theory Comput. 2017, 13, 265−273

Union's Horizon 2020 Research and Innovation program under Grant Agreements No. 676580 (NOMAD) and 646259 (MOSTOPHOS). H.H. acknowledges support from the People Programme (Marie Curie Actions) of the European Union's Seventh Framework Programme FP7-PEOPLE-2013-IEF project No. 622934.

Notes

The authors declare no competing financial interest.

REFERENCES

(1) Hüfner, S. *Photoelectron Spectroscopy*; Advanced Texts in Physics; Springer Berlin, Heidelberg: Berlin, Heidelberg, 2003.
(2) Damascelli, A.; Hussain, Z.; Shen, Z.-X. *Rev. Mod. Phys.* **2003**, *75*, 473.
(3) Krausz, F.; Stockman, M. I. *Nat. Photonics* **2014**, *8*, 205.
(4) Sánchez-Barriga, J.; Golias, E.; Varykhalov, A.; Braun, J.; Yashina, L. V.; Schumann, R.; Minár, J.; Ebert, H.; Kornilov, O.; Rader, O. *Phys. Rev. B: Condens. Matter Mater. Phys.* **2016**, *93*, 155426.
(5) Lisowski, M.; Loukakos, P. A.; Melnikov, A.; Radu, I.; Ungureanu, L.; Wolf, M.; Bovensiepen, U. *Phys. Rev. Lett.* **2005**, *95*, 137402.
(6) Cavalieri, A. L.; Müller, N.; Uphues, T.; Yakovlev, V. S.; Baltuska, A.; Horvath, B.; Schmidt, B.; Blümel, L.; Holzwarth, R.; Hendel, S.; Drescher, M.; Kleineberg, U.; Echenique, P. M.; Kienberger, R.; Krausz, F.; Heinzmann, U. *Nature* **2007**, *449*, 1029.
(7) Rohwer, T.; Hellmann, S.; Wiesenmayer, M.; Sohrt, C.; Stange, A.; Slomski, B.; Carr, A.; Liu, Y.; Avila, L. M.; Kalläne, M.; Mathias, S.; Kipp, L.; Rossnagel, K.; Bauer, M. *Nature* **2011**, *471*, 490.
(8) Neppl, S.; Ernstorfer, R.; Cavalieri, A. L.; Lemell, C.; Wachter, G.; Magerl, E.; Bothschafter, E. M.; Jobst, M.; Hofstetter, M.; Kleineberg, U.; Barth, J. V.; Menzel, D.; Burgdörfer, J.; Feulner, P.; Krausz, F.; Kienberger, R. *Nature* **2015**, *517*, 342.
(9) Bertoni, R.; Nicholson, C. W.; Waldecker, L.; Hübener, H.; Monney, C.; De Giovannini, U.; Puppin, M.; Hoesch, M.; Springate, E.; Chapman, R. T.; Cacho, C.; Wolf, M.; Rubio, A.; Ernstorfer, R. *arxiv:1606.03218* 2016; https://arxiv.org/abs/1606.03218.
(10) Hsieh, D.; Xia, Y.; Qian, D.; Wray, L.; Dil, J. H.; Meier, F.; Osterwalder, J.; Patthey, L.; Checkelsky, J. G.; Ong, N. P.; Fedorov, A. V.; Lin, H.; Bansil, A.; Grauer, D.; Hor, Y. S.; Cava, R. J.; Hasan, M. Z. *Nature* **2009**, *460*, 1101.
(11) Hsieh, D.; Xia, Y.; Wray, L.; Qian, D.; Pal, A.; Dil, J. H.; Osterwalder, J.; Meier, F.; Bihlmayer, G.; Kane, C. L.; Hor, Y. S.; Cava, R. J.; Hasan, M. Z. *Science* **2009**, *323*, 919.
(12) Xu, S.-Y.; Xia, Y.; Wray, L. A.; Jia, S.; Meier, F.; Dil, J. H.; Osterwalder, J.; Slomski, B.; Bansil, A.; Lin, H.; Cava, R. J.; Hasan, M. Z. *Science* **2011**, *332*, 560.
(13) Jozwiak, C.; Park, C.-H.; Gotlieb, K.; Hwang, C.; Lee, D.-H.; Louie, S. G.; Denlinger, J. D.; Rotundu, C. R.; Birgeneau, R. J.; Hussain, Z.; Lanzara, A. *Nat. Phys.* **2013**, *9*, 293.
(14) Pendry, J. B. *Surf. Sci.* **1976**, *57*, 679.
(15) Berglund, C. N.; Spicer, W. E. *Phys. Rev.* **1964**, *136*, A1030.
(16) Mahan, G. D.; Plummer, E. W. In *Handbook of Surface Science*; Horn, K., Scheffler, M., Eds.; Elsevier, 2000; pp 1−35.
(17) Korringa, J. *Physica* **1947**, *13*, 392.
(18) Kohn, W.; Rostoker, N. *Phys. Rev.* **1954**, *94*, 1111.
(19) Ebert, H.; Ködderitzsch, D.; Minár, J. *Rep. Prog. Phys.* **2011**, *74*, 096501.
(20) Uimonen, A. M.; Stefanucci, G.; van Leeuwen, R. *J. Chem. Phys.* **2014**, *140*, 18A526.
(21) Moritz, B.; Devereaux, T. P.; Freericks, J. K. *Phys. Rev. B: Condens. Matter Mater. Phys.* **2010**, *81*, 165112.
(22) Sentef, M.; Kemper, A. F.; Moritz, B.; Freericks, J. K.; Shen, Z.-X.; Devereaux, T. P. *Phys. Rev. X* **2013**, *3*, 041033.
(23) Braun, J.; Rausch, R.; Potthoff, M.; Minár, J.; Ebert, H. *Phys. Rev. B: Condens. Matter Mater. Phys.* **2015**, *91*, 035119.
(24) Tao, L.; Scrinzi, A. *New J. Phys.* **2012**, *14*, 013021.
(25) Scrinzi, A. *New J. Phys.* **2012**, *14*, 085008.
(26) Majety, V. P.; Zielinski, A.; Scrinzi, A. *J. Phys. B: At., Mol. Opt. Phys.* **2015**, *48*, 025601.
(27) Majety, V. P.; Zielinski, A.; Scrinzi, A. *New J. Phys.* **2015**, *17*, 063002.
(28) Zielinski, A.; Majety, V. P.; Nagele, S.; Pazourek, R.; Burgdörfer, J.; Scrinzi, A. *Phys. Rev. Lett.* **2015**, *115*, 243001.
(29) Zielinski, A.; Majety, V. P.; Scrinzi, A. *Phys. Rev. A: At., Mol., Opt. Phys.* **2016**, *93*, 023406.
(30) Wopperer, P.; De Giovannini, U.; Rubio, A. *arxiv:1608.02818* 2016, https://arxiv.org/abs/1608.02818.
(31) Einstein, A. *Ann. Phys.* **1905**, *322*, 132.
(32) Grigorenko, A. N.; Polini, M.; Novoselov, K. S. *Nat. Photonics* **2012**, *6*, 749.
(33) Lischner, J.; Vigil-Fowler, D.; Louie, S. G. *Phys. Rev. Lett.* **2013**, *110*, 146801.
(34) Caruso, F.; Giustino, F. *Phys. Rev. B: Condens. Matter Mater. Phys.* **2015**, *92*, 045123.
(35) Höfer, U.; Shumay, I. L.; Reuß, C.; Thomann, U.; Wallauer, W.; Fauster, T. *Science* **1997**, *277*, 1480.
(36) von Barth, U.; Hedin, L. *J. Phys. C: Solid State Phys.* **1972**, *5*, 1629.
(37) Giuliani, G. F.; Vignale, G. *Quantum theory of the electron liquid*; Cambridge Univ. Press: Cambridge, 2005.
(38) Runge, E.; Gross, E. *Phys. Rev. Lett.* **1984**, *52*, 997.
(39) Marques, M. A. L.; Maitra, N. T.; Nogueira, F.; Gross, E.; Rubio, A. *Fundamentals of Time-Dependent Density Functional Theory*; Springer-Verlag, 2011.
(40) Baer, R., Kronik, L., Kümmel, S. Eds. *Open problems and new solutions in time dependent density functional theory*; Chemical Physics 1; Elsevier, 2011; Vol. *391*; pp 1−176.
(41) Kohn, W. *Rev. Mod. Phys.* **1999**, *71*, 1253.
(42) Marques, M. A. L.; Bertsch, G. F.; Rubio, A. *Comput. Phys. Commun.* **2003**, *151*, 60.
(43) Castro, A.; Appel, H.; Oliveira, M. J. T.; Rozzi, C. A.; Andrade, X.; Lorenzen, F.; Marques, M. A. L.; Gross, E.; Rubio, A. *Phys. Status Solidi B* **2006**, *243*, 2465.
(44) Strubbe, D.; De Giovannini, U.; Larsen, A. H.; Varas, A.; Theophilou, I.; Helbig, N.; Verstraete, M. J.; Stella, L.; Aspuru-Guzik, A.; Castro, A. *Phys. Chem. Chem. Phys.* **2015**, *17*, 31371.
(45) Rozzi, C. A.; Varsano, D.; Marini, A.; Gross, E.; Rubio, A. *Phys. Rev. B: Condens. Matter Mater. Phys.* **2006**, *73*, 205119.
(46) Natan, A.; Benjamini, A.; Naveh, D.; Tiago, M.; Beckman, S.; Chelikowsky, J. R. *Phys. Rev. B: Condens. Matter Mater. Phys.* **2008**, *78*, 075109.
(47) Hartwigsen, C.; Goedecker, S.; Hutter, J. *Phys. Rev. B: Condens. Matter Mater. Phys.* **1998**, *58*, 3641.
(48) Perdew, J. P. *Phys. Rev. B: Condens. Matter Mater. Phys.* **1981**, *23*, 5048.
(49) Kübler, J.; Höck, K. H.; Sticht, J.; Williams, A. R. *J. Phys. F: Met. Phys.* **1988**, *18*, 469.
(50) Larsen, A. H.; De Giovannini, U.; Rubio, A. *Density-Functional Methods for Excited States*; Springer International Publishing: Cham, 2015; pp 219−271.
(51) De Giovannini, U.; Larsen, A. H.; Rubio, A. *Eur. Phys. J. B* **2015**, *88*, 1.
(52) Bostwick, A.; Ohta, T.; Seyller, T.; Horn, K.; Rotenberg, E. *Nat. Phys.* **2007**, *3*, 36.
(53) Mucha-Kruczyński, M.; Tsyplyatyev, O.; Grishin, A.; McCann, E.; Fal'ko, V. I.; Bostwick, A.; Rotenberg, E. *Phys. Rev. B: Condens. Matter Mater. Phys.* **2008**, *77*, 195403.
(54) Andrade, X.; Castro, A.; Zueco, D.; Alonso, J. L.; Echenique, P.; Falceto, F.; Rubio, A. *J. Chem. Theory Comput.* **2009**, *5*, 728.
(55) Riley, J. M.; Mazzola, F.; Dendzik, M.; Michiardi, M.; Takayama, T.; Bawden, L.; Granerod, C.; Leandersson, M.; Balasubramanian, T.; Hoesch, M.; Kim, T. K.; Takagi, H.; Meevasana, W.; Hofmann, P.; Bahramy, M. S.; Wells, J. W.; King, P. D. C. *Nat. Phys.* **2014**, *10*, 835.
(56) Riley, J. M.; Meevasana, W.; Bawden, L.; Asakawa, M.; Takayama, T.; Eknapakul, T.; Kim, T. K.; Hoesch, M.; Mo, S. K.; Takagi, H.; Sasagawa, T.; Bahramy, M. S.; King, P. D. C. *Nat. Nanotechnol.* **2015**, *10*, 1043.

DOI: 10.1021/acs.jctc.6b00897
J. Chem. Theory Comput. 2017, 13, 265−273

(57) Usachov, D.; Fedorov, A.; Vilkov, O.; Adamchuk, V. K.; Yashina, L. V.; Bondarenko, L.; Saranin, A. A.; Grüneis, A.; Vyalikh, D. V. *Phys. Rev. B: Condens. Matter Mater. Phys.* **2012**, *86*, 155151.
(58) Kronik, L.; Stein, T.; Refaely-Abramson, S.; Baer, R. *J. Chem. Theory Comput.* **2012**, *8*, 1515−1531.
(59) Refaely-Abramson, S.; Jain, M.; Sharifzadeh, S.; Neaton, J. B.; Kronik, L. *Phys. Rev. B: Condens. Matter Mater. Phys.* **2015**, *92*, 081204.
(60) Malet, F.; Mirtschink, A.; Mendl, C. B.; Bjerlin, J.; Karabulut, E. Ö.; Reimann, S. M.; Gori-Giorgi, P. *Phys. Rev. Lett.* **2015**, *115*, 033006.

DOI: 10.1021/acs.jctc.6b00897
J. Chem. Theory Comput. 2017, 13, 265−273